Proceedings of the Institution of Civil Engineers
Water Management 157
December 2004 Issue WM4
Pages 197–210

Paper 13567
Received 21/01/2004
Accepted 31/08/2004

Keywords:
coastal engineering/hydraulics & hydrodynamics/mathematical modelling

Müsteyde B. Koçyigit
Lecturer in Civil Engineering, Gazi University, Maltepe, Ankara, Turkey

Roger A. Falconer
Halcrow Professor of Environmental Water Management, Cardiff University, UK

ice

Modelling of wind-induced currents in water basins

M. B. Koçyigit PhD, MSc and R. A. Falconer PhD, DSc, DEng, FICE, FREng, FCGI, FCIWEN, FASCE

This paper presents a numerical modelling study into wind-induced currents in shallow water basins. A three-dimensional, semi-implicit, finite difference numerical model is described, incorporating non-hydrostatic pressure, based on a sigma-transformed system in the vertical direction. The numerical model was first validated for sloshing in a rectangular tank; excellent agreement was obtained against analytical solutions, provided the non-hydrostatic pressure is incorporated. The model was further verified against experimental data on wind-induced circulation in shallow rectangular tanks. It was then used to simulate wind-induced, three-dimensional flow fields in idealised rectangular tanks. A parameter study was carried out for wind-induced flows in Esthwaite Water, and the predictions compared against field data. It is shown that the numerical model is capable of accurately simulating the wind-induced circulation in shallow enclosed water bodies and that the topography and wind stress are of primary importance. The non-hydrostatic pressure does not have a significant effect on the wind-induced flow fields considered herein.

1. INTRODUCTION

In the last two decades, an increasing practical interest in water circulation in reservoirs and lakes has arisen due to the problems of water quality encountered in these water bodies from which water is supplied for either domestic or industrial use. This interest has led to the development of many numerical models because of the unavailability of analytical solutions of the mathematical equations that model water quality in shallow water. The formulation of the mathematical model in the co-ordinate system adopted is based on the physical properties of the flow domain and realistic assumptions.[1] Hence, a large variety of numerical models have been developed over the years. In the early 1980s, two-dimensional (2-D) models which are computationally efficient and easily implemented were successfully used to predict the flow field and the distribution of pollutants.[2–4] However, it was soon recognised that the 2-D models were not appropriate to simulate wind-induced circulation because of their inability to describe the three-dimensional (3-D) flow field. Furthermore, the bed stress calculation performed in 2-D models is physically unrealistic because the bed stress cannot be adequately parameterised in terms of depth-averaged velocity. In order to include vertical variations in the overall solution accuracy, 3-D models such as multi-layer models[5] and quasi-3-D models,[6] have been developed, producing variations in current and concentration through the vertical as well as in the horizontal. In order to increase the prediction capability of 3-D models, a large variety of numerical solution schemes,[7,8] orthogonal[9] and non-orthogonal grid transformations,[10] quad-tree mesh generation techniques[11] and substructuring techniques[12] have been developed over the years using various assumptions and simplifications.

The aim of this study was to develop a 3-D numerical model which is capable of simulating the 3-D effects of wind-induced currents and flow over complex bathymetry and to predict how the physical changes might alter the circulation pattern. The non-hydrostatic pressure distribution was also incorporated into the model equations to take into account the possible impact of vertical acceleration on the current structure and thereby on the circulation pattern where complex bathymetric changes may cause such phenomena.

2. GENERAL FORM OF MATHEMATICAL FORMULATION

The mathematical model is based on the governing equations that are derived by means of conservation laws for mass and momentum which are known as the Reynolds-averaged Navier–Stokes equations. After resolving the pressure term into hydrostatic (i.e. $\boldsymbol{P}_{\mathrm{h}} = \rho \boldsymbol{g}(\eta - z)$) and hydrodynamic (i.e. $\boldsymbol{P}_{\mathrm{dyn}} = \boldsymbol{q}$) components and introducing the notation of the eddy viscosity coefficient, the momentum equations for an incompressible fluid can be expressed in a fully conservative form as

$$1 \quad \frac{\partial \boldsymbol{u}}{\partial t} + \frac{\partial(\boldsymbol{uu})}{\partial x} + \frac{\partial(\boldsymbol{vu})}{\partial y} + \frac{\partial(\boldsymbol{wu})}{\partial z} = f\boldsymbol{v} - \boldsymbol{g}\frac{\partial \eta}{\partial x} - \frac{1}{\rho}\frac{\partial \boldsymbol{q}}{\partial x} + \frac{\partial}{\partial x}\left(\boldsymbol{\nu}_{\mathrm{h}}\frac{\partial \boldsymbol{u}}{\partial x}\right) + \frac{\partial}{\partial y}\left(\boldsymbol{\nu}_{\mathrm{h}}\frac{\partial \boldsymbol{u}}{\partial y}\right) + \frac{\partial}{\partial z}\left(\boldsymbol{\nu}_{\mathrm{v}}\frac{\partial \boldsymbol{u}}{\partial z}\right)$$

$$2 \quad \frac{\partial \boldsymbol{v}}{\partial t} + \frac{\partial(\boldsymbol{uv})}{\partial x} + \frac{\partial(\boldsymbol{vv})}{\partial y} + \frac{\partial(\boldsymbol{wv})}{\partial z} = -f\boldsymbol{u} - \boldsymbol{g}\frac{\partial \eta}{\partial y} - \frac{1}{\rho}\frac{\partial \boldsymbol{q}}{\partial y} + \frac{\partial}{\partial x}\left(\boldsymbol{\nu}_{\mathrm{h}}\frac{\partial \boldsymbol{v}}{\partial x}\right) + \frac{\partial}{\partial y}\left(\boldsymbol{\nu}_{\mathrm{h}}\frac{\partial \boldsymbol{v}}{\partial y}\right) + \frac{\partial}{\partial z}\left(\boldsymbol{\nu}_{\mathrm{v}}\frac{\partial \boldsymbol{v}}{\partial z}\right)$$

$$3 \quad \frac{\partial \boldsymbol{w}}{\partial t} + \frac{\partial(\boldsymbol{uw})}{\partial x} + \frac{\partial(\boldsymbol{vw})}{\partial y} + \frac{\partial(\boldsymbol{ww})}{\partial z} = -\frac{1}{\rho}\frac{\partial \boldsymbol{q}}{\partial z} + \frac{\partial}{\partial x}\left(\boldsymbol{\nu}_{\mathrm{h}}\frac{\partial \boldsymbol{w}}{\partial x}\right) + \frac{\partial}{\partial y}\left(\boldsymbol{\nu}_{\mathrm{h}}\frac{\partial \boldsymbol{w}}{\partial y}\right) + \frac{\partial}{\partial z}\left(\boldsymbol{\nu}_{\mathrm{v}}\frac{\partial \boldsymbol{w}}{\partial z}\right)$$

where x, y and z are the Cartesian coordinates oriented

eastward, northward, and upward, respectively; $\boldsymbol{u}$, $\boldsymbol{v}$ and $\boldsymbol{w}$ are the velocity components in the horizontal x, y and the vertical z-directions; η is the water surface above horizontal datum ($z = 0$ at the undisturbed water surface); $\boldsymbol{q}$ is the non-hydrostatic pressure component; t is the time; $\boldsymbol{g}$ is the gravitational acceleration; ρ is the fluid density; f is the Coriolis parameter; $\boldsymbol{\nu}_h$ and $\boldsymbol{\nu}_v$ are the kinematic eddy viscosity coefficients in the horizontal and vertical directions, respectively.

Likewise, the conservation of mass may be expressed through the continuity equation which can be written for an incompressible flow as

$$\frac{\partial \boldsymbol{u}}{\partial x}+\frac{\partial \boldsymbol{v}}{\partial y}+\frac{\partial \boldsymbol{w}}{\partial z}=0 \tag{4}$$

An equation for free surface evolution is derived by integrating the continuity equation (4) over the depth and applying the Leibniz rule giving

$$\frac{\partial \eta}{\partial t}+\frac{\partial}{\partial x}\left[H\int_{-1}^{0}\boldsymbol{u}d\boldsymbol{\sigma}\right]+\frac{\partial}{\partial y}\left[H\int_{-1}^{0}\boldsymbol{v}d\boldsymbol{\sigma}\right]=0 \tag{5}$$

where H is the total depth of water column.

To define bed and surface boundaries accurately, the sigma co-ordinate system is used in the vertical direction. The numerical mesh thus fits the free surface and bed very closely enabling a higher resolution near boundaries where sharp velocity gradients may be observed. The horizontal gradients of the non-hydrostatic pressure $\boldsymbol{q}$ and the horizontal diffusion terms in equations (1)–(3) are not transformed into the sigma co-ordinate system in order to avoid large errors, especially near steep bottom slopes where small pressure gradients might be the result of the sum of two relatively large terms of opposite sign, resulting in a relatively large error in the pressure gradient that can induce artificial flows.[13,14] Details of the transformation and resulting equations can be found in Koçyigit.[15]

3. NUMERICAL SOLUTION METHOD

A fractional step method was used to solve the 3-D free surface flow equations in two steps.[16] For the first step the gradient of the surface elevation in the horizontal momentum equations and the horizontal velocities in the surface equation are discretised using the θ-method.[17] In the momentum equations, the vertical viscosity terms are dicretised implicitly for stability, whereas the rest of the terms, namely the advection, Coriolis and horizontal viscosity terms, are discretised explicitly. The non-hydrostatic pressure is also included in the momentum equations to incorporate the effects of the hydrodynamic pressure distribution on the free-surface elevation. For the discretisation of the equations, a conventional staggered mesh system was used. The centre of the cells was numbered with indices i, j, k, where $i = 1,\ldots, I$, $j = 1,\ldots, J$ and $k = 1,\ldots, K$, with $k = 1$ for the surface cell and $k = K$ for the bed cell. The $\boldsymbol{u}$-velocity was then defined at $(i + 1/2, j, k)$; the velocity $\boldsymbol{v}$ was defined at $(i, j + 1/2, k)$ and the vertical velocities $\boldsymbol{w}$ and $\boldsymbol{\omega}$ were defined at the node $(i, j, k - 1/2)$. The hydrodynamic pressure term $\boldsymbol{q}$ was defined at the node (i, j, k), the surface elevation η was defined at the cell centre (i, j) and the water depth $H(x, y)$ was specified at the centre of each grid side, that is $(i + 1/2, j)$ and $(i, j + 1/2)$, thereby providing a comprehensive representation of the bathymetry. Thus, after discretisation of the horizontal momentum equations and substitution of the horizontal velocities from the discretised momentum equations into the discretised free surface equation, the free surface equation is obtained in the following form[18]

$$\begin{aligned}
&\eta_{i,j}^{n+1}-\boldsymbol{g}\theta^2\frac{\Delta t^2}{\Delta x^2}\left\{\left[(\Delta\boldsymbol{\sigma})^{\mathrm{T}}\mathrm{A}^{-1}\Delta\boldsymbol{\sigma}\right]_{i+1/2,j}^{n}(\eta_{i+1,j}^{n+1}-\eta_{i,j}^{n+1})\right.\\
&\left.-\left[(\Delta\boldsymbol{\sigma})^{\mathrm{T}}\mathrm{A}^{-1}\Delta\boldsymbol{\sigma}\right]_{i-1/2,j}^{n}(\eta_{i,j}^{n+1}-\eta_{i-1,j}^{n+1})\right\}\\
&-\boldsymbol{g}\theta^2\frac{\Delta t^2}{\Delta y^2}\left\{\left[(\Delta\boldsymbol{\sigma})^{\mathrm{T}}\mathrm{A}^{-1}\Delta\boldsymbol{\sigma}\right]_{i,j+1/2}^{n}(\eta_{i,j+1}^{n+1}-\eta_{i,j}^{n+1})\right.\\
&\left.-\left[(\Delta\boldsymbol{\sigma})^{\mathrm{T}}\mathrm{A}^{-1}\Delta\boldsymbol{\sigma}\right]_{i,j-1/2}^{n}(\eta_{i,j}^{n+1}-\eta_{i,j-1}^{n+1})\right\}\\
&\quad=\delta_{i,j}^{n}-\frac{\Delta t}{\Delta x}\left\{\left[(\Delta\boldsymbol{\sigma})^{\mathrm{T}}\mathrm{A}^{-1}\mathrm{G}\right]_{i+1/2,j}^{n}-\left[(\Delta\boldsymbol{\sigma})^{\mathrm{T}}\mathrm{A}^{-1}\mathrm{G}\right]_{i-1/2,j}^{n}\right\}\\
&\qquad-\frac{\Delta t}{\Delta y}\left\{\left[(\Delta\boldsymbol{\sigma})^{\mathrm{T}}\mathrm{A}^{-1}\mathrm{G}\right]_{i,j+1/2}^{n}-\left[(\Delta\boldsymbol{\sigma})^{\mathrm{T}}\mathrm{A}^{-1}\mathrm{G}\right]_{i,j-1/2}^{n}\right\}
\end{aligned} \tag{6}$$

where $\mathrm{G}_{i+1/2,j}^{n}$ and $\mathrm{G}_{i,j+1/2}^{n}$ contain all of the explicit terms, $\mathrm{A}_{i+1/2,j}^{n}$ and $\mathrm{A}_{i,j+1/2}^{n}$ contain the coefficients of the unknown velocities and $\Delta\boldsymbol{\sigma}_{i+1/2,j}^{n}$ and $\Delta\boldsymbol{\sigma}_{i,j+1/2}^{n}$ contain the layer thickness in the discretised momentum equations in the x- and y-directions, respectively.

This five-diagonal system of equations, with the unknowns $\tilde{\boldsymbol{u}}_{i+1/2,j,k}^{n+1}$, $\tilde{\boldsymbol{v}}_{i,j+1/2,k}^{n+1}$ and $\eta_{i,j}^{n+1}$ being specified over the entire computational mesh, has to be solved at each time step to determine recursively values of the field variables. Once the new surface elevation is determined, the discretised momentum equations are solved to determine the horizontal velocity field. With the help of a flag introduced in the code, the model can be run with or without the hydrostatic assumption. If the model is run without the hydrostatic assumption, then the vertical momentum equation is used to determine the intermediate vertical velocity field. Otherwise the vertical velocity $\boldsymbol{w}$ at the new time level $n + 1$ is to be found from the continuity equation.

In the second step the new velocity fields $\boldsymbol{u}_{i+1/2,j,k}^{n+1}$, $\boldsymbol{v}_{i,j+1/2,k}^{n+1}$ and $\boldsymbol{w}_{i,j,k+1/2}^{n+1}$ are computed by correcting the intermediate velocity field ($\tilde{\boldsymbol{u}}_{i+1/2,j,k}^{n+1}$, $\tilde{\boldsymbol{v}}_{i,j+1/2,k}^{n+1}$ and $\tilde{\boldsymbol{w}}_{i,j,k+1/2}^{n+1}$) with the gradient of the hydrodynamic pressure correction term, since the intermediate velocity field will not satisfy the local continuity equation. Hence, the hydrodynamic pressure correction term is determined by requiring that the new velocity field is convergent. Defining $\boldsymbol{q}$ as the hydrodynamic pressure correction term, the discrete momentum equations therefore become

$$\boldsymbol{u}_{i+1/2,j,k}^{n+1}=\tilde{\boldsymbol{u}}_{i+1/2,j,k}^{n+1}-\frac{\Delta t}{\Delta x}(\boldsymbol{q}_{i+1,j,k}^{\prime n+1}-\boldsymbol{q}_{i,j,k}^{\prime n+1}) \tag{7}$$

$$\boldsymbol{v}_{i,j+1/2,k}^{n+1}=\tilde{\boldsymbol{v}}_{i,j+1/2,k}^{n+1}-\frac{\Delta t}{\Delta y}(\boldsymbol{q}_{i,j+1,k}^{\prime n+1}-\boldsymbol{q}_{i,j,k}^{\prime n+1}) \tag{8}$$

$$\boldsymbol{w}_{i,j,k+1/2}^{n+1}=\tilde{\boldsymbol{w}}_{i,j,k+1/2}^{n+1}-\frac{\Delta t}{H_{i,j}^{n}\Delta\boldsymbol{\sigma}_{k+1/2}}(\boldsymbol{q}_{i,j,k}^{\prime n+1}-\boldsymbol{q}_{i,j,k+1}^{\prime n+1}) \tag{9}$$

In each computational grid the incompressibility condition should be satisfied.[19] The expressions for the new velocities from equations (7) to (9) are therefore substituted into the

discretised incompressibility equation, resulting in the following finite difference Poisson equation for the hydrodynamic pressure correction term

$$10\quad \begin{aligned}&\frac{\Delta t}{\Delta x^2}\Delta\sigma^n_{i+1/2,j,k}(q'^{n+1}_{i+1,j,k}-q'^{n+1}_{i,j,k})\\&-\frac{\Delta t}{\Delta x^2}\Delta\sigma^n_{i+1/2,j,k}(q'^{n+1}_{i,j,k}-q'^{n+1}_{i-1,j,k})\\&+\frac{\Delta t}{\Delta y^2}\Delta\sigma^n_{i,j+1/2,k}(q'^{n+1}_{i,j+1,k}-q'^{n+1}_{i,j,k})\\&-\frac{\Delta t}{\Delta y^2}\Delta\sigma^n_{i,j+1/2,k}(q'^{n+1}_{i,j,k}-q'^{n+1}_{i,j-1,k})\\&+\frac{1}{\Delta\sigma^n_{i,j,k-1/2}}(q'^{n+1}_{i,j,k-1}-q'^{n+1}_{i,j,k})\\&-\frac{1}{\Delta\sigma^n_{i,j,k+1/2}}(q'^{n+1}_{i,j,k}-q'^{n+1}_{i,j,k+1})\\&\quad=\frac{1}{\Delta x}\left[\Delta\sigma^n_{i+1/2,j,k}\tilde{u}^{n+1}_{i+1/2,j,k}-\Delta\sigma^n_{i-1/2,j,k}\tilde{u}^{n+1}_{i-1/2,j,k}\right]\\&\qquad+\frac{1}{\Delta y}\left[\Delta\sigma^n_{i,j+1/2,k}\tilde{v}^{n+1}_{i,j+1/2,k}-\Delta\sigma^n_{i,j-1/2,k}\tilde{v}^{n+1}_{i,j-12/,k}\right]\\&\qquad+\left[\tilde{w}^{n+1}_{i,j,k-1/2}-\tilde{w}^{n+1}_{i,j,k+1/2}\right]\end{aligned}$$

Thus, equation (10) forms a seven-diagonal linear system that is solved iteratively by the conjugate gradient method. Once the hydrodynamic pressure correction term is computed, the final velocity field at the new time level is determined from equations (7) to (9) and the hydrodynamic pressure field is updated with the hydrodynamic pressure correction term.

The system of equations is subject to various types of boundary conditions. At the solid impermeable boundaries, no mass flux is allowed through the boundary and therefore zero normal flow is imposed in equations (7) to (9). For the pressure Poisson equation (10), a Neumann type of boundary condition is used. At the surface, the hydrodynamic pressure $\boldsymbol{q}$ is set to zero, so a Dirichlet type of boundary condition is specified in equation (10). For the case of a wind stress on the surface, the shear stress at the free surface is taken equal to the wind stress. At the free surface $\boldsymbol{q}=0$ and $\boldsymbol{w}$ is determined in a surface cell by applying the continuity equation (4). At the bed, the impermeability condition is applied, wherein $\omega^{n+1}_{i,j,k+1/2}=0$.

Since the θ-method is used in the model, it is important to decide the value of θ to be used in the numerical model. When $\theta=1$, the algorithm becomes fully implicit and wave damping problems may arise. To avoid damping and ensure high accuracy and efficiency, a semi-implicit scheme is used where $\theta=1/2$ so that the average values of the pressure gradient and the velocities are used in the momentum equations and free surface equation. Details of the stability analysis, the accuracy and the efficiency of a semi-implicit finite difference scheme can be found in Casulli and Cattani.[17]

4. MODEL VERIFICATION AND APPLICATION

4.1. Comparison with analytical solutions

First, a small amplitude wave test case was performed to test mass and energy conservation and to demonstrate the effects of the hydrodynamic pressure on the circulation pattern. For this test, a uni-nodal standing wave was simulated in a closed flat-bottomed square basin of length 10 m and depth 10 m containing inviscid liquid of constant density. The initial free surface elevation had a cosine distribution, and the initial velocity field was zero everywhere. The amplitude of the wave was taken to be 0·1 m, 1% of the water depth, enabling the application of the small amplitude wave theory.[20] The basin was discretised with 400 square cells, of grid side 0·5 m and the time step was 0·001 s to enable a high accuracy. Comparisons of model predictions with analytical solutions were performed for free surface elevation, velocity field and hydrodynamic pressure distribution in the section at the centre of the basin in the depth direction and presented for the same phases of motion of $t=3T/8$ in Fig. 1. The comparisons showed very good agreement between the analytical solutions and the numerical results. Furthermore, it was shown in Fig. 2 that the model with the hydrostatic approximation yielded long-wave velocity profiles, which were not realistic and physically not correct, compared with the physically correct and smooth velocity profiles obtained using the non-hydrostatic pressure algorithm. Details of the small amplitude wave theory, its analytical solution and the test case can be found in Jankowski[21] and Koçyigit.[15]

Another comparison of the model predictions to an analytical solution was performed for a steady wind-driven circulatory flow in a closed basin with a flat bed and with linearised bottom friction. The advection, Coriolis, horizontal diffusion and cross (y-direction) terms were neglected, leading to a balance between the surface gradient, the vertical diffusion of momentum, the surface wind stress and the bottom friction term in the momentum equation. The analytic solution for a constant vertical eddy viscosity and linearised bottom friction is[22]

$$11\quad \boldsymbol{u}=\frac{1}{6\boldsymbol{\nu}_v}\boldsymbol{g}\frac{\partial\xi}{\partial x}\left(3z^2-H^2\right)+\frac{\tau_w}{2\rho\boldsymbol{\nu}_v}(H+2z)$$

$$12\quad \frac{\partial\xi}{\partial x}=\frac{3}{2}\frac{\tau_w}{\rho\boldsymbol{g}H}\frac{(2\boldsymbol{\nu}_v+k_lH)}{(3\boldsymbol{\nu}_v+k_lH)}$$

where $\boldsymbol{u}$ is the horizontal velocity, ξ is the surface elevation, $\boldsymbol{\nu}_v$ is the vertical eddy viscosity, $\boldsymbol{g}$ is the acceleration due to gravity, τ_w is the wind stress, H is the water depth, ρ is the water density and k_l is the linearised bottom friction coefficient.

For this test case two steady wind conditions were applied, where the wind stress τ_w was set to 0·1 N/m^2 and 0·325 N/m^2, respectively. The other model parameters in the numerical simulations were: $H=40$ m, $\boldsymbol{g}=9{\cdot}81$ m/s^2, $\rho=1026$ kg/m^3, $\boldsymbol{\nu}_v=0{\cdot}03$ m^2/s and $k_l=0{\cdot}005$ m/s. The test basin was square, with an area of 12 km $\times$ 12 km and it was discretised with a square grid of side 1 km. The model was started with a zero velocity field and elevation and the simulation continued under constant wind forcing. Numerical simulations were first carried out with a uniform layer thickness in the depth direction and then by means of logarithmic distribution of layers the grid resolution was enhanced near the surface and bottom boundaries, where steep velocity gradients were expected due to the wind and bed shear stresses. Comparisons of the model predictions at the centre of the basin with the analytical solution for $\boldsymbol{W}=5$ m/s and $\boldsymbol{W}=10$ m/s for the case of uniformly distributed layers are shown in Fig. 3 where it can be seen that, as expected, the upper layer currents are in

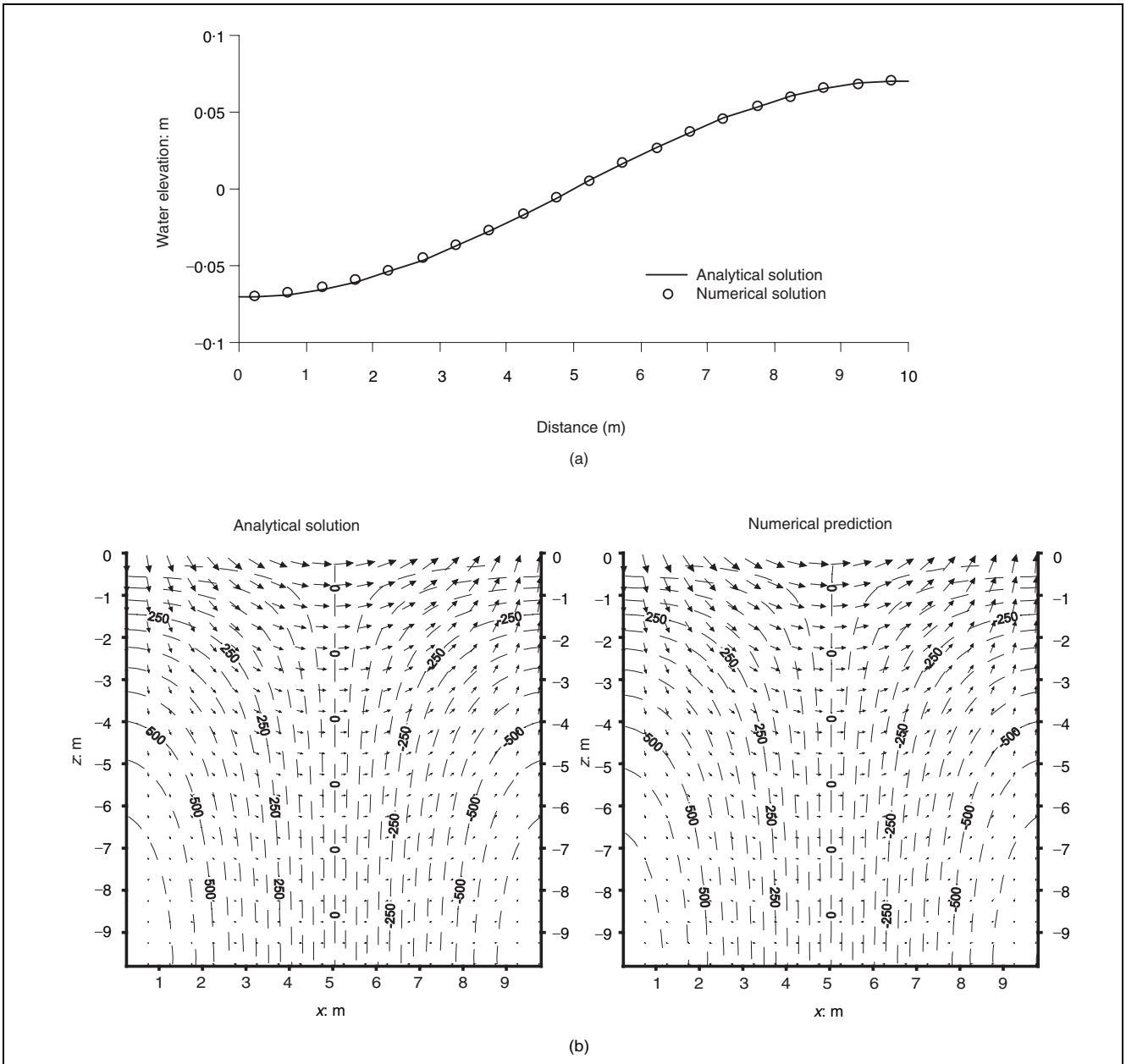

Fig. 1. Comparison between numerical and analytical solutions for phase angle of $t = 3T/8$ for: (a) free surface elevation; (b) velocity and hydrodynamic pressure fields in the vertical section

the wind direction whereas the lower layer currents are in the opposite direction, to maintain mass balance in the closed basin. Fig. 4 shows the numerical model predictions at the centre of the basin for five and 10 layers where the resolution near the surface and bed was enhanced by using a number of logarithmic distributions of layers and with uniformly distributed layers. The absolute error results also showed that the model predictions approached the analytic solution both when the number of layers was increased and when the layers were concentrated near the boundaries. For the case of evenly distributed layers, the predictions improved by up to 82% for the velocity in the first layer near the surface and 70% for the velocity near the bed, with the number of layers increasing from five to 10 and from five to 16, respectively. For the case of a logarithmic distribution of layers, a higher accuracy was obtained especially for the velocity near bed. For instance an improvement of up to 95% was obtained for the case of an increase in the number of layers from five to 16.

4.2. Verification using experimental data

The first set of experimental data used to validate the numerical model was acquired by Baines and Knapp,[23] whose experimental apparatus consisted of a wind channel with a uniform depth of 0·3048 m, 0·9144 m by 0·9144 m cross-section and 12·80 m long, which was covered for 9·144 m to produce a working section for the tests. Observations were made at 31 different points over the depth for two wind conditions with average wind speeds of about 6·73 and 6·90 m/s. The main experimental parameters and their results are presented in Table 1.

In the numerical model, the same conditions were deployed. The channel was discretised with square grid cells of side 0·18288 m and the time step was set to 1·2 s. Ten layers were used in the depth direction and the effect of the distribution of the layers was also investigated. Various algebraic equations and turbulence models such as the two-layer, mixing-length

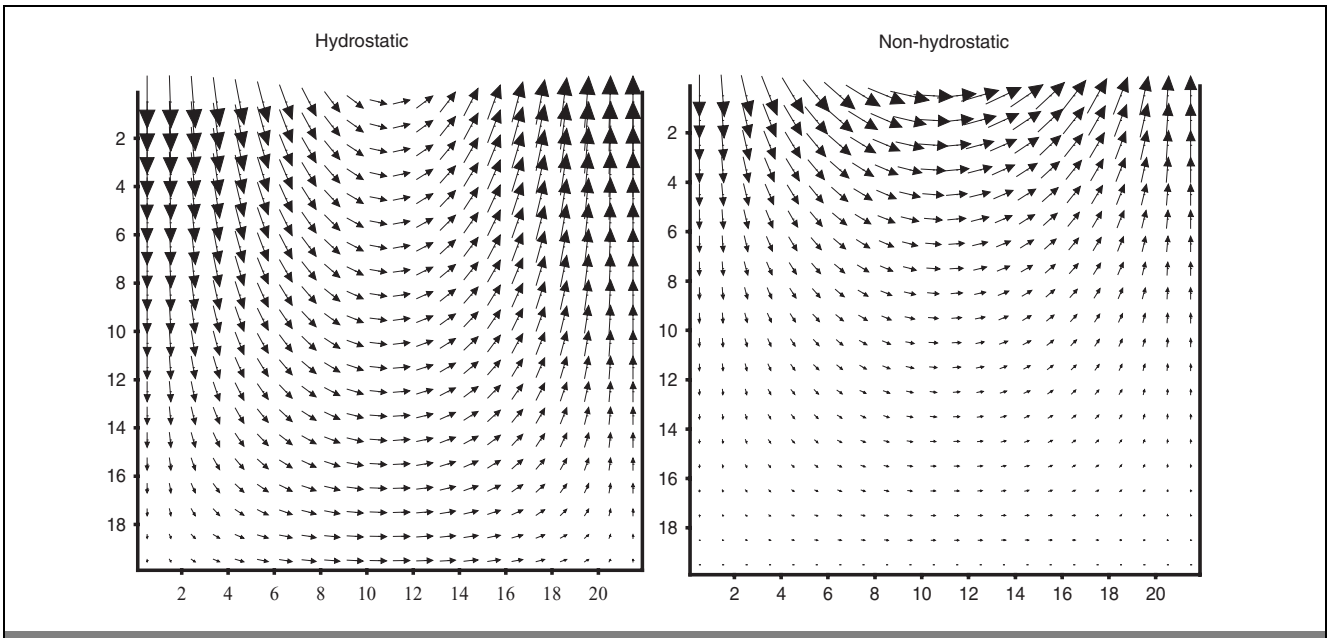

Fig. 2. Comparison of solutions at $T/4$, both with and without hydrostatic approximation

model, one- and two-equation turbulence models were implemented in the model to predict the vertical eddy viscosity distribution throughout the flow domain. For this set of experiments, the parabolic eddy viscosity distribution developed by Wu and Tsanis[24] was found to best simulate the wind-induced currents in the vertical section because it was also based on similar experimental data. Details of the turbulence models deployed can be found in Koçyigit.[15] Predicted velocity profiles normalised by the surface shear velocity, together with the experimental results, are presented in Fig. 5 for the two wind conditions, where the wind speed was 3·901 and 6·096 m/s, respectively. It can be seen from laboratory data that detailed currents were not measured close to the bed—that is, lower than 10% of the depth—and because of the limited number of measurements near the surface there was no appreciable difference between the profiles measured for the two Reynolds numbers. It was found from Fig. 5(a) and (b) that the model was able to simulate the velocity profile over depth to a reasonable level of accuracy.

Another experiment of wind-induced currents was performed by Tsuruya *et al.*[25] and was also used for the verification of the numerical model. A wind-wave tank with a constant depth of 0·15 m and a length of 22 m was used as the experimental apparatus. The tank was dicretised with seven square grids of spacing 0·2 m and the time step was taken to be 0·2 s. Fifteen

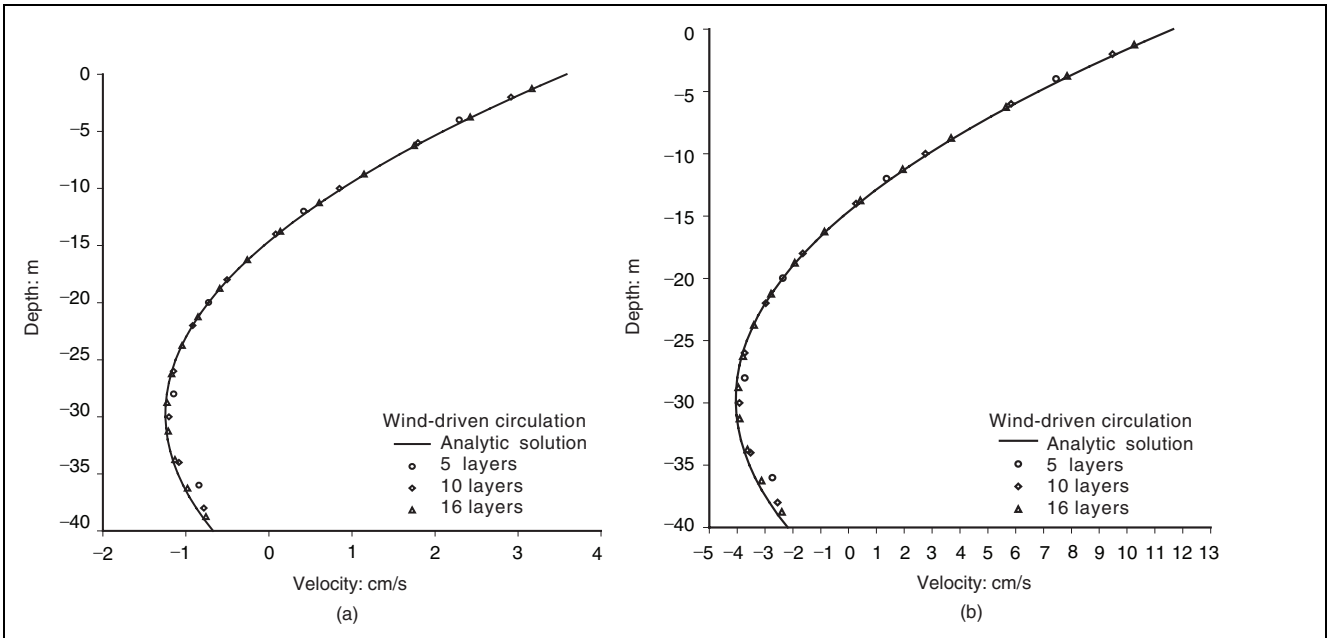

Fig. 3. Comparison of numerical model predictions with analytical solution at the centre of the basin in case of uniformly distributed layers for: (a) $W = 5$ m/s, (b) $W = 10$ m/s

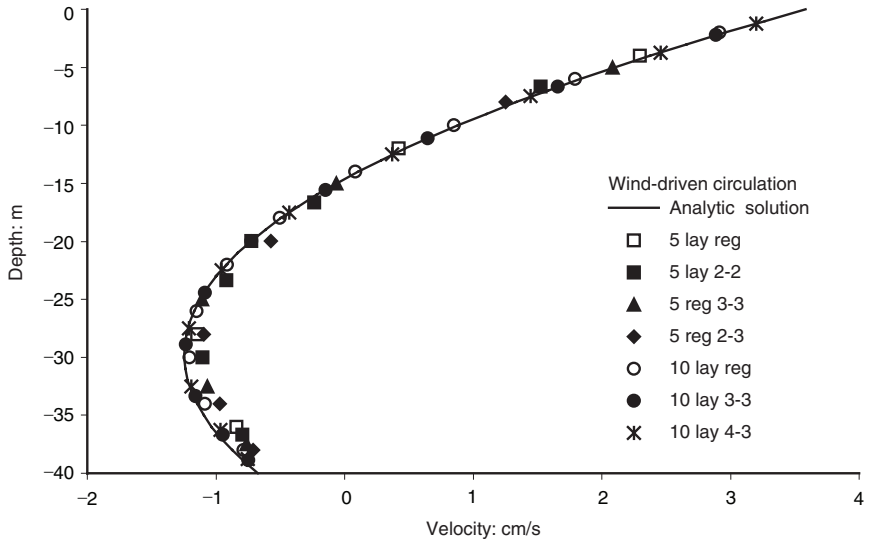

Fig. 4. Comparison of numerical model predictions with analytical solution for uniformly and various logarithmically distributed layers for $W = 5$ m/s ('lay' = layer; 'reg' = uniformly distributed layers; '4–3' = higher resolution near surface and near bed (logarithmically distributed 4 and 3 layers, respectively)

uniformly distributed layers were used over the depth. Two wind conditions, namely 6·73 and 6·90 m/s were used. Relevant experimental parameters are shown in Table 2.

The results of the numerical model and the experimental data are plotted in Fig. 6. It was observed that there was a noticeable agreement between the model simulations and the experimental data and it may therefore be concluded that the model is applicable to prototype cases.

4.3. Test cases under realistic conditions

The numerical model was then applied to two idealised rectangular basins, with sizes being close to those of a typical lake and for different bathymetric layouts to demonstrate the 3-D predictive capacity of the model and to investigate the influence of the bathymetry on the wind-induced circulation patterns. One of the basins (Basin A) had a constant depth whereas the other basin (Basin B) had a depth-varying bathymetry, as shown in Fig. 7. The length and the width of the basins were assumed to be 2·35 and 0·85 km respectively, and the mean depth was set to 15 m. The basin was discretised using a square grid of size 50 m with 15 uniformly distributed layers being used over the depth. The time step was set to 10 s. The model was started with a zero velocity field and it was assumed that the water was initially at rest. A westerly wind of 5 m/s, blowing from west to east, was introduced in both basins and the predicted velocity fields at various layers are illustrated in Fig. 8 after steady-state conditions had been reached. As seen in Fig. 8(a) and (b), there is a striking difference in the predicted circulation pattern, demonstrating the influence of the bathymetry on the velocity field across the basin. Two symmetric gyres, one clockwise and one anticlockwise, are formed in Basin B due to the bathymetry whereas in Basin A no such pattern was observed.

4.4. Application to a small lake

As a practical case study, Esthwaite Water, a small but morphometrically complex shallow lake in Cumbria, UK, was chosen to assess the model capability of simulating the circulation patterns in a lake. Esthwaite Water has approximate dimensions of 2·3 km along the main axis, with a maximum width of 0·6 km and a maximum depth of nearly 16 m (Fig. 9). A programme of field measurements was undertaken by Hall[26] and took place during periods when the lake was in an

Quantity		Test 1	Test 2
(1)	(2)		
Depth	h: m	0·3048	0·3048
Wind velocity	$\boldsymbol{W}$: m/s	3·9010	6·0960
Surface shear velocity	$\boldsymbol{U}_{*s}$: cm/s	0·6233	0·9416
Surface velocity	$\boldsymbol{U}_s$: cm/s	10·7200	15·2500
Reynolds number	$R_s = \boldsymbol{u}_s h/\boldsymbol{v}$	32 700·0000	46 500·0000
Normalised surface velocity	$\boldsymbol{U}s/\boldsymbol{u}_{*s}$	17·2000	16·2000
Absolute roughness	Z_{ow}: mm	0·3521	0·4795

Table 1. Experimental parameters and results by Baines and Knapp[23]

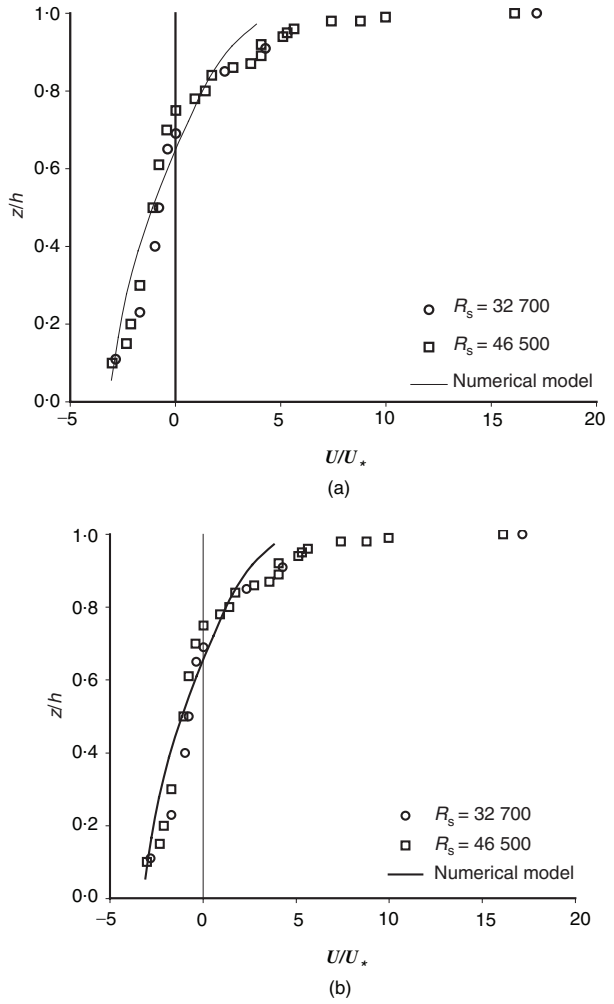

Fig. 5. Normalised velocity profiles in a channel of uniform depth for: (a) $W = 3{\cdot}901$ m/s; (b) $W = 6{\cdot}096$ m/s[23]

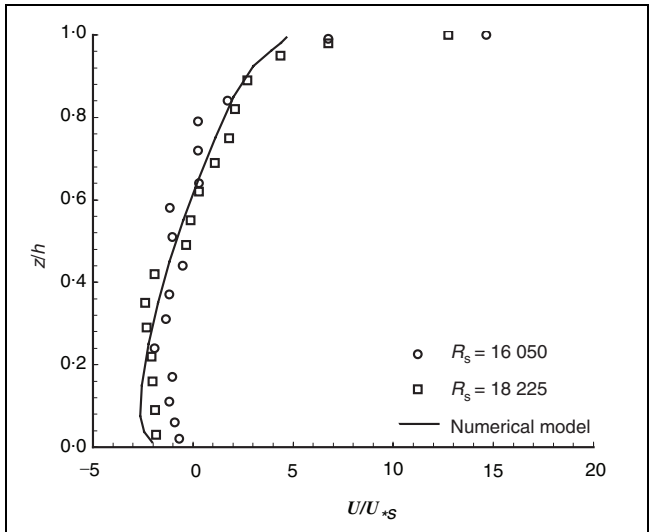

Fig. 6. Normalised velocity profiles: verification of 3-D model with experimental data[25]

isothermal state. Horizontal velocity profiles were obtained over the depth at many locations for wind conditions that produced a near steady-state circulation pattern. Details about the lake, the field study and the measurement techniques used can be found in Hall.[26] The numerical model was set up for Esthwaite Water in which the computational domain was set up with a horizontal mesh of 21×51 grid squares, with a uniform grid spacing of 50 m. The model was started with zero velocity fields and the steady-state condition was reached after about 8 h of simulation. The predictions were compared with measured velocity profiles at selected measurement sites in Esthwaite Water. The comparisons were achieved by resolving each horizontal velocity into its components along and perpendicular to the wind direction. Fig. 10 presents comparisons between the predicted and measured velocity profiles at two sites in open water for a 3 m/s wind blowing from a 340° wind angle where generally favourable agreement between both sets of results is found. Comparisons for a wind speed of 2·5 m/s blowing from 20° east of north and 6 m/s with a wind direction of 210° are presented in Fig. 11(a) and (b), respectively, with the numerically predicted currents being slightly lower than the measured currents. Stronger velocity components were reported along the wind axis whereas the slower velocity components were across the wind axis. This result suggested that the Coriolis force was influential in this small lake. However, comparisons in Fig. 11 also showed that lateral boundaries affected the currents in these near shore regions, where the Coriolis force was not effective and the continuity requirement generated a strong return current. The headlands and shoreline had a pronounced effect on the current structure, which was not well represented in the model. To improve on the predictions of the complex flow structure in the shallower regions close to the shore a finer horizontal mesh, which can be generated by an automatic mesh generation technique, is planned to be incorporated into the model at a later stage.

Quantity		Test 1	Test 2
(1)	(2)		
Depth	h: m	0·150	0·150
Wind velocity	$\boldsymbol{W}$: m/s	6·900	6·800
Surface shear velocity	$\boldsymbol{U}_{*s}$: cm/s	0·815	0·835
Surface velocity	$\boldsymbol{U}_s$: cm/s	10·700	12·150
Reynolds number	$R_s = \boldsymbol{u}_s h/\boldsymbol{v}$	16050·000	18225·000
Normalised surface velocity	$\boldsymbol{U}_s/\boldsymbol{u}_{*s}$	12·740	14·550
Absolute roughness	Z_{ow}: mm	0·210	0·360

Table 2. Experimental parameters and results by Tsuruya *et al.*[25]

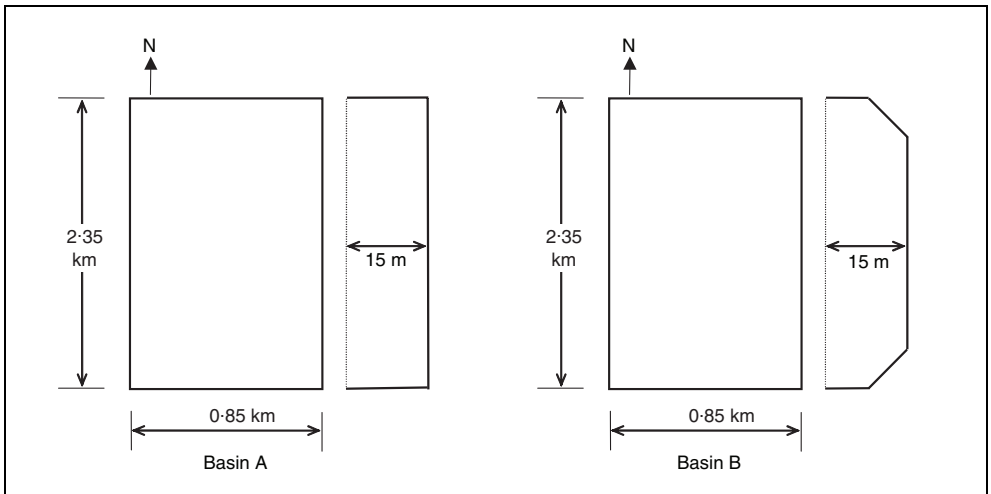

Fig. 7. Simplified rectangular basins and their topography

A series of simulations were also undertaken to examine the effects of several main model parameters on the circulation patterns across the entire lake and on the current structure over the depth. The main parameters considered to have a pronounced effect on the circulation were eddy viscosity, wind speed, wind direction and bed roughness. In addition to these main parameters, the air–water resistance coefficient and the hydrodynamic pressure component were also investigated.

First, a range of constant eddy viscosity coefficients and several turbulence models, of the one and two equation types, were deployed to predict the distribution of the vertical eddy viscosity coefficient. Further details of the turbulence models employed can be found in Koçyigit.[15] Numerical simulations showed that the eddy viscosity coefficient is of considerable importance in predicting the 3-D velocity structure of wind-induced circulation and that the more sophisticated turbulence models deployed did not produce any improvements in the results when compared with a simple turbulence model, as shown in Fig. 12. Therefore, in this study, the two-layer, mixing-length model was chosen because of its easy implementation and low computational cost to provide an acceptable level of accuracy. As would be expected, the wind speed and wind direction were also found to have a significant impact on the circulation as wind speed is directly proportional to the amount of energy put into the system. It was observed that the magnitude of the velocity field increased proportionally with increasing wind speed and that the size and location of eddies predicted changed noticeably with the wind direction.

Although the effect of the Coriolis acceleration in small lakes is usually inferred to be negligible, field observations and numerical simulations presented in Fig. 13 showed that the current deflections in Esthwaite Water were significant where the surface layer velocities were deflected to the right of the wind direction for the case with the Coriolis acceleration being included and therefore has a noticeable effect on the circulation patterns. George and Heaney[27] carried out a field study in Esthwaite Water and the measurements they took indicated that the current deflections in Esthwaite Water were significant.

Another important parameter is the air–water resistance coefficient which is used in the computation of surface shear stress when the wind acts on the water surface. Experiments show that the wind stress can be expressed in a quadratic equation, relating the stress to the wind velocity and the aerodynamic properties of the water surface.[28] Although a value of $2{\cdot}6 \times 10^{-3}$ proposed by Wilson (cited in Weiyan[29]) is widely used and also deployed in this study, numerous research studies have shown that the value of this resistance coefficient depends upon many parameters, but mainly wind speed. A variety of formulations[30–32] were tested and the simulations showed that the proposed equations in the literature are usually inaccurate for lakes and other inland water bodies, where the wind speed may be affected by surrounding topography, thereby leading to underestimated surface fluid velocities. In recent years, research has been conducted into adding air-water-coupled models to hydrodynamic numerical models in order to include the influences of sheltering effects and the air–water resistance coefficient on the wind field.[33,34]

The effect of the hydrodynamic pressure component was investigated on the circulation patterns across the entire lake and on the velocity structure at several sites by comparing the measured and predicted profiles of the horizontal velocities. Little effect of the hydrodynamic pressure was observed on the circulation patterns, as shown in Fig. 14. In comparing the velocity profile, the current site was chosen where the vertical acceleration could be more pronounced because of the presence of steep slopes at this site. Furthermore, the available data at this site were measured under the strongest wind measured in the lake during field studies, namely 7 m/s.

5. CONCLUSIONS

A 3-D numerical model has been developed to simulate wind-induced circulation in enclosed homogeneous water bodies such as lakes and reservoirs, especially with a complex bathymetry. A conventional sigma coordinate system was applied in the vertical direction to represent the bathymetry as accurately as possible, including the non-hydrostatic pressure distribution in the governing equations. A semi-implicit finite difference scheme was used and the hydrostatic and hydro-

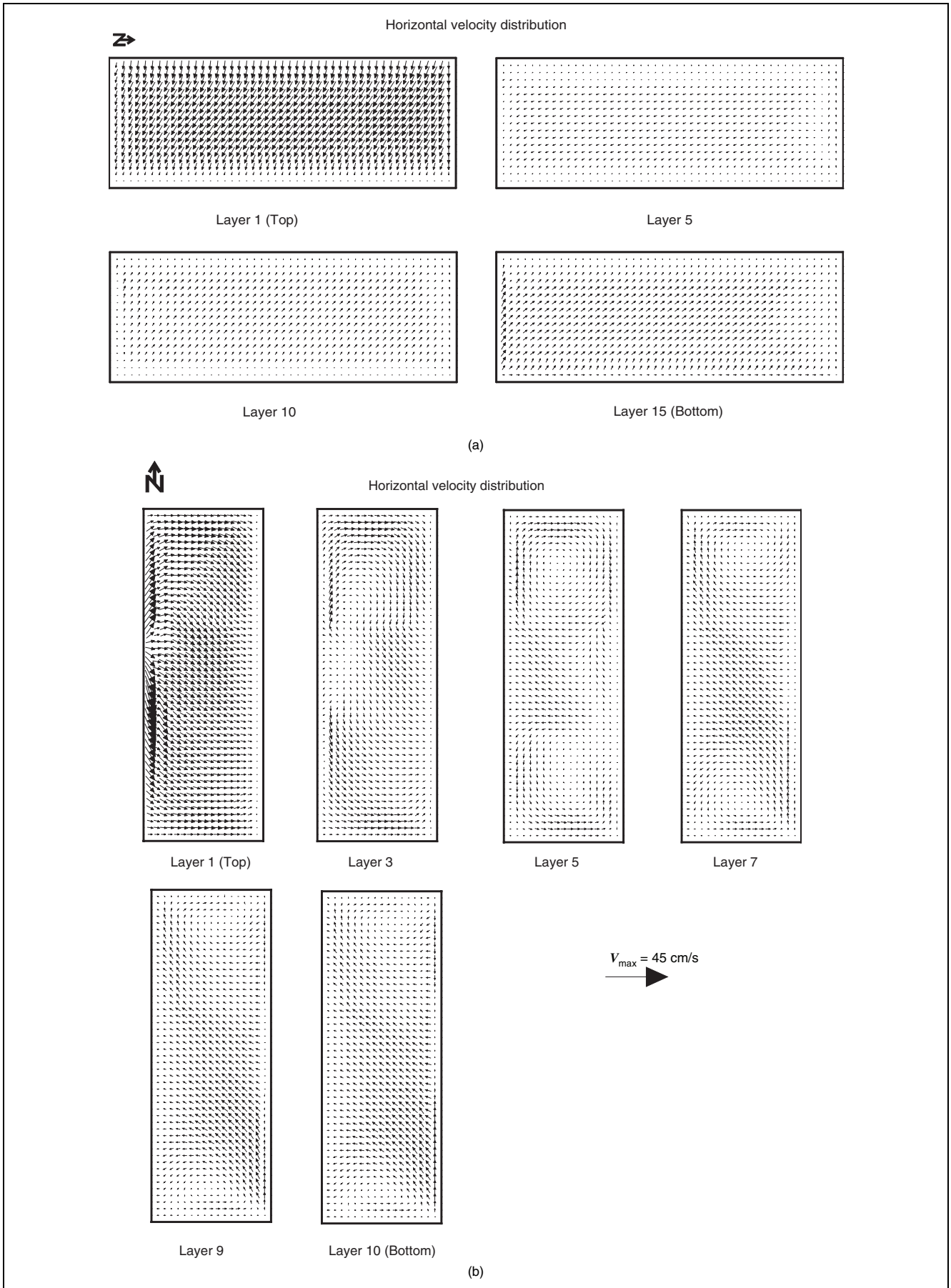

Fig. 8. Predicted circulation pattern in (a) Basin A; and (b) Basin B

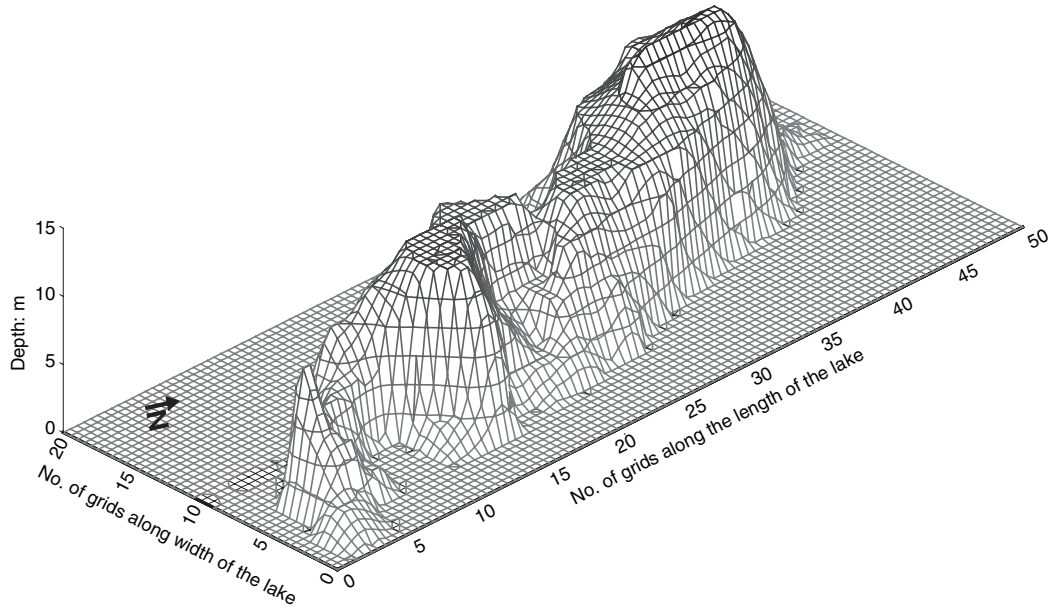

Fig. 9. Isometric plot of Esthwaite Water

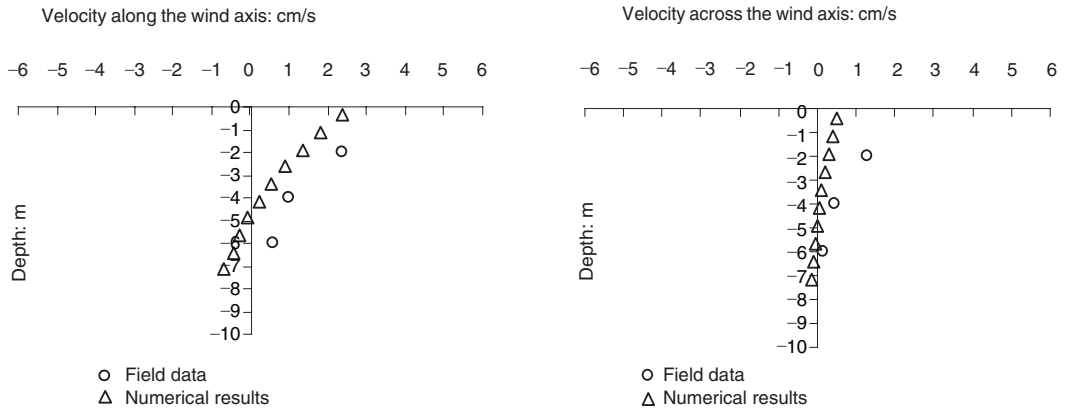

Fig. 10. Predicted and measured velocity profiles in open water in Esthwaite Water for a wind speed of 3 m/s

dynamic pressure components were computed at two stages, enabling the model to be run both with and without the hydrostatic pressure assumption.

The model was first tested against available analytical solutions for short-period surface wave sloshing and wind-induced currents in a closed basin of constant depth. It was shown that there was a very good agreement between analytical solutions and numerical model predictions in both cases, with the velocity structure over depth being well reproduced. Close agreement was achieved between the numerical predictions and published laboratory data, which demonstrated that the model was capable of simulating wind-induced currents properly. Following comparisons with analytical solutions and laboratory data, the numerical model was applied to two idealised rectangular basins having the same dimensions but different bathymetric layouts. It was found that different circulation patterns were obtained in these basins due to the influence of the bathymetry. Then, the numerical model was applied to Esthwaite Water, a small lake in Cumbria, UK. Simulations showed that the eddy viscosity coefficient, the wind speed and the wind direction are the main parameters affecting circulation and also that the Coriolis acceleration had a pronounced effect on the circulation patterns, except close to lateral boundaries. It was also discovered that the hydrodynamic pressure effect became significant at steep slopes near the shore. This requires further field investigation.

Further developments to the model would be to include the effects of lateral boundaries, thereby improving the shoreline representation, and to perform a wider range of field measurements covering the shore zone. Furthermore, the numerical model should also be applied to other lakes for further investigation of the circulation patterns, sensitivity of the model parameters and calibration and validation of the model.

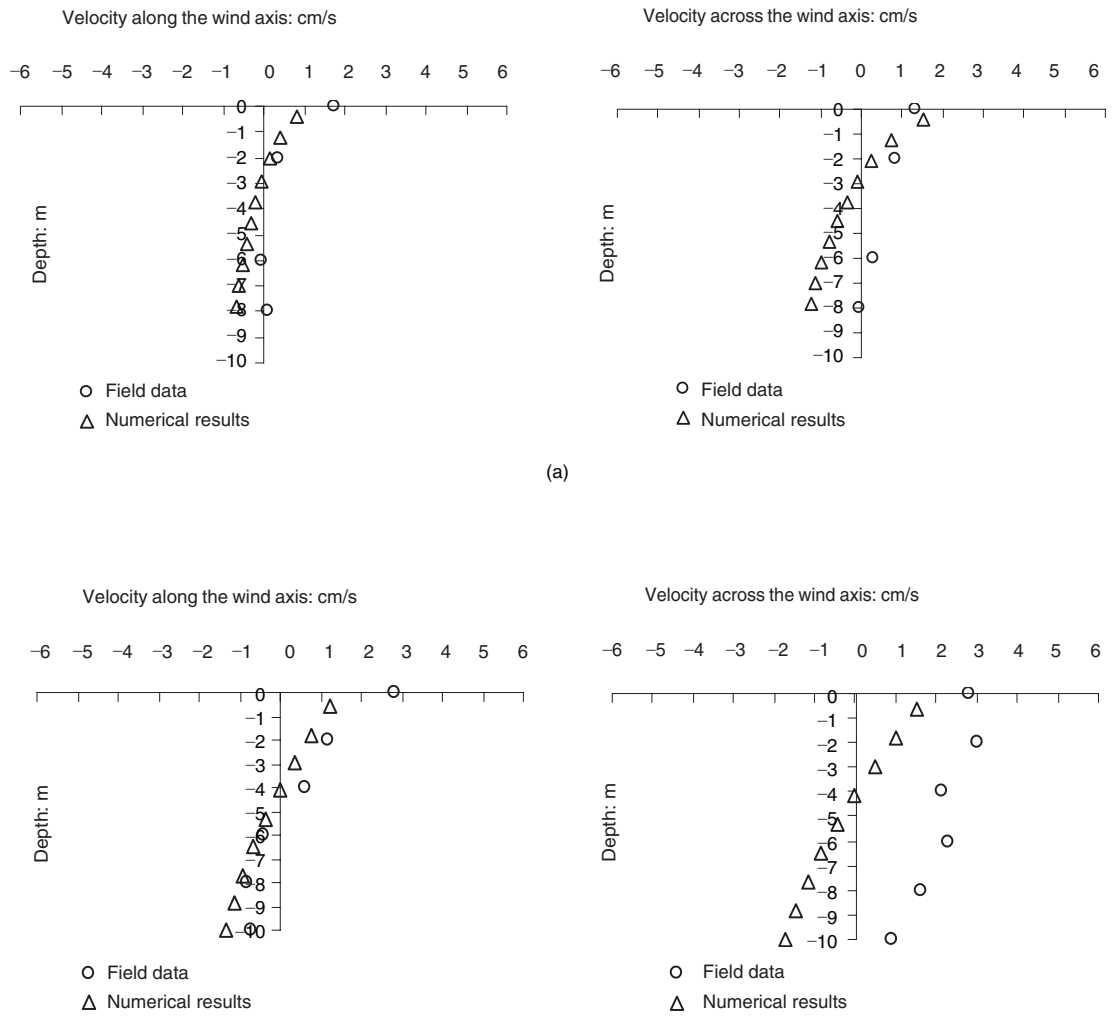

Fig. 11. Predicted and measured velocity profiles in sheltered water in Esthwaite Water for a wind speed of (a) 2·5 m/s; (b) 6 m/s

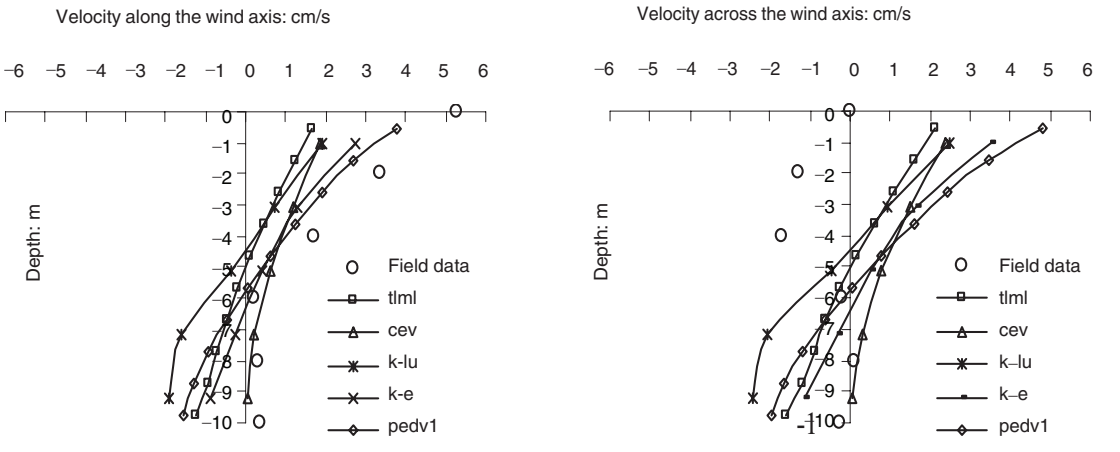

Fig. 12. Comparison between measured velocities and model predictions for a wind speed of 6 m/s with various turbulence models employed (tlml = two-layer mixing length model; cev = constant eddy viscosity; k–lu and k–e = one- and two-equation turbulence models; pedv1 = empirical equation)

Fig. 13. Predicted horizontal velocity field for surface layer with a wind speed of 3 m/s: (a) including the Coriolis acceleration; (b) neglecting the Coriolis acceleration

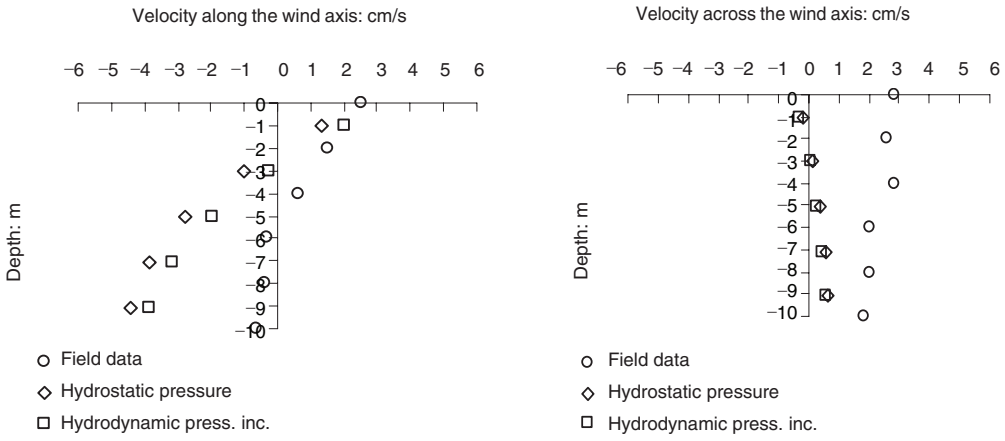

Fig. 14. Comparison between measured and predicted velocities for a northerly wind of 7 m/s

6. ACKNOWLEDGEMENTS

The authors are grateful to the Institute of Freshwater Ecology, for originally providing the hydrodynamic data for a Natural Environment Research Council CASE studentship. The authors also wish to thank Dr D. G. George from the Institute of Freshwater Ecology, for his assistance in providing the data.

REFERENCES

1. KOUTITAS C. and O'CONNOR B. Modelling three-dimensional wind-induced flows. *ASCE Journal of Hydraulic Division*, 1980, **106**, No. HY11, 1843–1865.
2. FALCONER R. A. Water quality simulation study of a natural harbour. *Journal of Waterway, Port, Coastal and Ocean Engineering*, 1986, **112**, No. 1, 15–34.
3. CHENG R. T., CASULLI V. and GARTNER J. W. Tidal, Residual, Inter-tidal Mudflat (TRIM) model and its applications to San Francisco Bay, California. *Estuarine, Coastal and Shelf Science*, 1993, **36**, 235–280.
4. HAYTER E. J., BERGS R. G. and MCCUTCHEON S. C. *HSCTM-2D, a Finite Element Model for Sediment and Contaminant Transport*. Draft Report, US Environmental Protection Agency, Athens, GA, 1997.
5. FALCONER R. A. An introduction to nearly horizontal flows. In *Coastal, Estuarial and Harbour Engineers' Reference Book* (ABBOTT M. B. and PRICE W. A. (eds)). F. N. Spon, London, 1993, ch. 2, pp. 27–36.
6. KOUTITAS C. and GOUSIDOU-KOUTITA M. A comparative study of three mathematical models for wind-generated circulation in coastal areas. *Coastal Engineering*, 1986, **10**, 127–138.
7. SIMONS T. J. *Circulation Models of Lakes and Inland Seas*. Canadian Bulletin of Fisheries and Aquatic Sciences, Bulletin 203, Department of Fisheries and Oceans, Ottawa, 1980.
8. SHENG Y. P. Modelling hydrodynamics and water quality dynamics in shallow waters. Keynote Paper. *Proceedings of an International Symposium on Ecology and Engineering*, Taman Negara, Malaysia, 1–4 November, 1994.
9. HAMRICK J. *A Three Dimensional Model of Turkey Creek and Adjacent Indian Lagoon*. Technical Report, Virginia Institute of Marine Science, 1994.
10. BORTHWICK A. G. L. and BARBER R. W. River and reservoir flow modelling using the transformed shallow water equations. *International Journal for Numerical Methods in Fluids*, 1992, **14**, 1193–1217.
11. BORTHWICK A. G. L., CRUZ LEÓN S. and JÓZSA J. Adaptive quad tree model of shallow-flow hydrodynamics. *Journal of Hydraulic Research*, 2001, **39**, No. 4, 413–424.
12. WANG Y. and HUTTER K. Methods of sub structuring in lake circulation dynamics. *Advances in Water Resources*, 2000, **23**, 399–425.
13. HANEY R. L. On the pressure gradient force over steep topography in sigma co-ordinate ocean models. *AMS Journal of Physical Oceanography*, 1991, **21**, No. 4, 610–619.
14. STELLING G. S. and VAN KESTER J. A. Th. M. On the approximation of horizontal gradients in sigma co-ordinates for bathymetry with steep bottom slopes. *International Journal for Numerical Methods in Fluids*, 1994, **18**, 915–935.
15. KOÇYIGIT M. B. *Numerical Modelling of Wind-induced Circulation in Lakes and Reservoirs*. PhD Thesis, Cardiff University, UK, 2002.
16. CASULLI V. and CHENG R. T. Semi-implicit finite difference methods for three-dimensional shallow water flow. *International Journal for Numerical Methods in Fluids*, 1992, **15**, 629–648.
17. CASULLI V. and CATTANI E. Stability, accuracy and efficiency of a semi-implicit method for three dimensional shallow water flow. *Computers and Mathematics with Applications*, 1994, **27**, No. 4, 99–112.
18. KOÇYIGIT M. B., FALCONER R. A. and LIN B. Three-dimensional numerical modelling of free surface flows with non-hydrostatic pressure. *International Journal for Numerical Methods in Fluids*, 2002, **40**, 1145–1162.
19. CASULLI V. and STELLING G. S. Numerical simulation of three dimensional, quasi-hydrostatic free-surface flows. *ASCE Journal of Hydraulic Engineering*, 1998, **124**, No. **7**, 678–686.
20. LEBLOND P. and MYSAK L. *Waves in the Ocean*, Elsevier Oceanography Series 20. Elsevier, Amsterdam-Oxford-New York, 1978, 602 pp.
21. JANKOWSKI J. A. *A Non-hydrostatic Model for Free Surface Flows*. PhD Thesis, Hannover University, Germany, 1999.
22. HUANG W. and SPAULDING M. 3D model of estuarine circulation and water quality induced by surface discharges. *ASCE Journal of Hydraulic Engineering*, 1995, **121**, No. 4, 300–311.
23. BAINES W. D. and KNAPP D. J. Wind driven water currents. *Journal of the Hydraulic Division, Proceedings of the ASCE,* 1965, **9**, No. 4, 343–358.
24. WU J. and TSANIS I. K. A vertical/horizontal integration wind-induced circulation model: a method for including surface and bottom logarithmic profiles. *Advances in Water Resources*, 1995, **18**, 77–87.
25. TSURUYA H., NAKAMO S. and KATO H. Experimental study on wind driven current in a wind-wave tank-effect of return flow on wind driven current. In *The Ocean Surface*. 1985, 425–430.
26. HALL P. *Numerical Modelling of Wind-induced Lake Circulation*. PhD Thesis, University of Birmingham, UK, 1987.
27. GEORGE D. G. and HEANEY S. I. Factors influencing the spatial distribution of phytoplankton in a small productive lake. *Journal of Ecology*, 1978, **66**, 133–155.
28. RAMMING H. G. and KOWALIK Z. *Numerical Modelling of Marine Hydrodynamics: Applications to Dynamic Physical Processes*, Elsevier Oceanography Series 26. Elsevier/North-Holland Inc., Amsterdam, 1980.
29. WEIYAN T. *Shallow Water Hydrodynamics*. Elsevier, Amsterdam, the Netherlands, 1992.
30. DEACON E. L. and WEBB K. E. Interchange of properties between sea and air: small scale interactions. In *The Sea* (HILL M. N. (ed.)). Inter Science, 1962, **1**, 43–87.
31. WU J. Wind-stress coefficients over sea surface from breeze to hurricane. *Journal of Geophysical Research*, 1982, **87**, 9704–9706.
32. WAMDI GROUP. The WAM model a third generation ocean wave prediction model. *Journal of Physical Oceanography*, 1988, **18**, No.12, 1775–1810.

33. JINXIU L., SHUKUN L., SHUJUN L. and XUEZHONG Y. Numerical modelling of wind-induced currents in shallow lakes. In *Environmental Hydraulics* (LEE J. H. W., JAYAWARDENA A. W. and WANG Z. Y. (eds)). 1999.

34. YANG J. S., HUANG W. G. and ZHOU C. B. Retrieval of ocean surface wind stress and drag coefficient from spaceborne SAR. *Progress in Natural Science*, 2001, **11**, No. 5, 397–400.

Please email, fax or post your discussion contributions to the secretary by 1 June 2005: email: kathleen.hollow@ice.org.uk; fax: +44 (0)20 7665 2294; or post to Kathleen Hollow, Journals Department, Institution of Civil Engineers, 1–7 Great George Street, London SW1P 3AA.